Natural halloysite nanotubes supported Ru as highly active catalyst for photothermal catalytic CO$_2$ reduction

Kang Peng [a,b], Jingying Ye [a], Hongjie Wang [a,*], Hui Song [b,*], Bowen Deng [b,c], Shuang Song [b,e], Yihan Wang [a], Linjie Zuo [a], Jinhua Ye [b,c,d,**]

[a] State Key Laboratory for Mechanical Behavior of Materials, Xi'an Jiaotong University, Xi'an 710049, China
[b] International Center for Materials Nanoarchitectonics (WPI-MANA), National Institute for Materials Science (NIMS), 1–1 Namiki, Tsukuba, Ibaraki 305–0044, Japan
[c] Graduate School of Chemical Sciences and Engineering, Hokkaido University, Sapporo, 060–0814, Japan
[d] TJU-NIMS International Collaboration Laboratory, School of Material Science and Engineering, Tianjin University, Tianjin 300072, China
[e] College of Carbon Neutrality Future Technology, Sichuan University, Chengdu 610065, China

ARTICLE INFO

ABSTRACT

Photothermal catalytic CO$_2$ reduction has emerged as a promising approach to efficiently utilize solar energy and reduce greenhouse gas emissions. Designing novel catalyst with high activity and selectivity is essential and challenging for practical applications of photothermal CO$_2$ reduction. Herein, we report that natural halloysite nanotubes-supported Ru nanoparticles can boost the photothermal catalytic activity and selectivity of CO$_2$ methanation under continuous flow conditions. The photothermal catalytic performance of optimized catalyst is up to 1704 mmolCH$_4$ g$_{cat}^{-1}$ h^{-1} with 93% CH$_4$ selectivity and 68% CO$_2$ conversion, outperforming any other Ru-based catalysts in photothermal CO$_2$ reduction. Mechanistic studies show that the outstanding catalytic performance is mainly attributed to the unique mesoporous tubular structure, excellent ability of light-to-heat and interfacial interactions between the halloysite nanotubes and Ru. This method of utilizing natural minerals as support provides a facile avenue for rational design of abundant and low-cost catalysts for efficient photothermal catalytic CO$_2$ reduction.

1. Introduction

In the past 60 years, the CO$_2$ concentration in the global atmosphere increases sharply by about 100 ppm due to the consumption of fossil fuels, leading to an increasingly serious greenhouse effect and ocean acidification [1,2]. The catalytic reduction of CO$_2$ to high-value chemicals and fuels is of great significance to mitigating climate change, environmental issues and energy crisis [3–5]. Among various strategies of CO$_2$ reduction, catalytic CO$_2$ methanation (Sabatier reaction: CO$_2$ + 4 H$_2$ → CH$_4$ + 2 H$_2$O) with hydrogen from renewable energy is a potential approach to industrial application for its economic and technical practicality and proven natural gas system [6–8], which is also considered as an alternative to hydrogen storage and utilization. Photothermal catalysis driven by solar energy presents the advantages of excellent adjustability, high activity and energy utilization in the field of catalytic CO$_2$ methanation [9–12]. The development of low-cost and high-efficiency

photothermal catalytic materials under flow conditions is critical for the future industrial application of CO$_2$ reduction [13–16].

Among various inspected photothermal catalysts for CO$_2$ methanation, ruthenium (Ru)-based materials have been extensively studied owe to its excellent catalytic selectivity and activity [17]. The support materials have significant impacts on the catalytic performance for CO$_2$ methanation for Ru-based catalysts [18,19]. An amount of support materials are applied to construct Ru-based composite catalytic materials for high-efficiency CO$_2$ methanation, such as Si [20], Al$_2$O$_3$[21–23], CeO$_2$[24,25], BN [26], and TiO$_2$ [27,28]. Typically, Ye et al. [29] reported that Ru supported on Mg-Al layered double hydroxides exhibited high photothermal catalytic activity for CO$_2$ methanation under continuous flow conditions, which was attributed to targeting activation of H$_2$ and CO$_2$ on Ru and layered double hydroxides. Ozin et al.[30,31] reported that Ru and RuO$_2$ were supported on silicon nanowire and silicon photonic crystal for photothermal CO$_2$ reduction,

in which the high light harvesting properties of silicon support materials could enhance the photomethanation rates. The construction of appropriate support materials for Ru-based catalysts is an effective approach to achieve efficient photothermal CO_2 methanation.

As an abundantly available and low-price natural clay mineral [32, 33], halloysite possesses the special morphology of hollow nanotubes [34], the wall of which is consisting of unit layers with one tetrahedral layer (SiO_4) and one octahedral layer (AlO_6)[35]. The external diameter of halloysite nanotubes (HNT) is about 50–150 nm, and their length is about 200–1000 nm [36]. The high specific surface area, adsorption ability, physicochemical properties and availability as well as cost and environmental advantages make natural halloysite appealing for a wide range of applications [37,38]. Moreover, the special nanotube morphology of halloysite could induce excellent gas permeability and light absorption, which is beneficial for gas-phase photothermal catalysis [39]. Therefore, natural halloysite is a promising support material for photothermal catalytic reactions but remains largely unexplored.

In this study, we demonstrate that Ru nanoparticles supported on natural HNT (Ru/HNT) by a facile wet impregnation method is a highly active catalyst for photothermal catalytic CO_2 reduction to CH_4. The high specific surface area and mesoporous tubular structure provide good adsorption capacity of CO_2 and allow enhanced light absorption. Moreover, due to the unique chemical properties of HNT, Ru/HNT interfaces create a strong electronic interaction to promote catalytic CO_2 reduction. As a result, a high catalytic activity of 1704 $mmolCH_4\ g_{cat}^{-1}\ h^{-1}$ for photothermal CO_2 methanation with 93% selectivity was obtained under 2.05 W cm^{-2} light irradiation in a flow system, corresponding to 68% single-pass CO_2 conversion. The high catalytic activity and cost advantage of Ru/HNT heralds promising prospects in large-scale application of photothermal CO_2 methanation. Meanwhile, this study provides a guideline for rational design of photothermal catalytic support materials.

2. Experimental section

2.1. Materials

The natural clay minerals of halloysite nanotubes (HNT), kaolinite nanorods (KNR) and nanosheets (KNS) were obtained from Hunan and Guangdong Province, China. Ruthenium chloride trihydrate ($RuCl_3·3$ H_2O) was purchased from Sigma-Aldrich. Acetone (C_3H_6O), aluminium oxide (Al_2O_3), silicon dioxide (SiO_2), hydrochloric acid (HCl) and sodium hydroxide (NaOH) were purchased from Wako.

2.2. Catalyst preparation

The catalysts were synthesized via a facile wet impregnation method. Typically, 54 mg of HNT was immersed in 5 mL of $RuCl_3$/acetone solution with stirring for 24 h, and the acetone solvent was evaporated to gain powders. The catalyst of Ru supported on HNT with the typical loading amount of 3 wt% was obtained after calcined under H_2 atmosphere at 400 °C for 4 h. Meanwhile, the different Ru weight loading on HNT (1–9 wt%) were performed, respectively. In the surface acid and alkali treatments of HNT, 250 mg of HNT was immersed in 25 mL of 3 M HCl or 3 M NaOH solution at 80 °C for 6 h, respectively. For comparison, Ru was loaded on KNR, KNS, commercial SiO_2 and Al_2O_3 with the loading amount of 3 wt% via similar method, and the corresponding catalysts was denoted as Ru/KNR, Ru/KNS, Ru/SiO_2 and Ru/Al_2O_3, respectively.

2.3. Characterization methods

The morphologies of catalysts were observed with a field emission scanning electron microscopy (FESEM, GeminiSEM 500) and transmission electron microscopy (TEM, JEM-F200). XRD (PANalytical) and XPS (Thermo Fisher ESCALAB Xi+) were used to determine the

crystallographic structures and chemical states. UV–vis–NIR absorption spectra were measured on a spectrophotometer (PE Lambda950). N_2 adsorption-desorption isotherms were measured on a Micromeritics ASAP 2020. The FTIR spectra were performed on a VERTEX70 FTIR spectrometer. The H_2 temperature-programmed reduction and CO_2 temperature-programmed desorption were conducted on a chemisorption Analyzer (AutoChem1 II 2920) with a thermal conductivity detector. For H_2 temperature-programmed reduction, the dried sample was flushed after cooled to 25 °C under flowing He, and reduced with 50 mL min^{-1} of 10% H_2/Ar with a heating rate of 5 °C min^{-1}. For CO_2 temperature-programmed desorption, the sample was flushed with 50 mL min^{-1} of 10% CO_2/He for 1 h after cooled to 25 °C under flowing He. Subsequently, the sample was purged with 50 mL min^{-1} of He for 1 h to remove weakly adsorbed CO_2, and then heated to 800 °C with a heating rate of 5 °C min^{-1}. In-situ DRIFTS measurements were carried out with an FT-IR-6300 system (JASCO Corp.).

2.4. Catalytic performance tests

The photothermal catalytic CO_2 reduction under continuous flow conditions was carried out in a photo-reactor with a 300 W Xe lamp as the light source. Reactant gas mixtures of CO_2 (5 mL min^{-1}) and H_2 (20 mL min^{-1}) under ambient pressure and 5 mg of catalyst were used in all experiments. A thermocouple was placed into the catalyst to measure the real-time temperature of the catalyst bed during the photothermal catalytic process. The temperature distribution of catalyst surface was monitored with an infrared thermograph (Fotric 285, China). The effluent reaction products were analyzed regularly by using a Shimadzu GC-2014 C gas chromatograph after the temperature of the catalyst bed stabilized. The photo-assisted thermocatalytic CO_2 reduction under continuous flow conditions was carried out in an electric heating reactor with same reactant gas mixtures and 5 mg of catalyst. The temperature of the catalyst bed was controlled by a TC-1000 controller. A LA-251Xe lamp (Hayashi) with L42 + HA30 filters was equipped on the electric heating reactor to analyze the photothermal enhancement effect. Density functional theory (DFT) calculations were performed to analyze the catalytic mechanism, and the calculation method [40,41] is included in the supplementary material.

3. Results and discussion

3.1. Photothermal catalytic performance

The synthesis of Ru/HNT was realized via a simple impregnation method (Fig. 1a) with Ru weight loading of 3%. For comparison, the other two natural clay materials, kaolinite nanorods (KNR) and kaolinite nanosheets (KNS) were used to support Ru nanoparticles (denoted as Ru/KNR and Ru/KNS, respectively). The photothermal catalysis was performed under continuous flow conditions (Fig. S1) with an inlet gas flow rate of 25 mL min^{-1} (CO_2/H_2 =1/4) under different light intensities. Bare clay minerals (HNT, KNR and KNS) without Ru exhibit negligible photothermal catalytic activity, indicating the critical role of Ru in photothermal CO_2 reduction. Similarly, without light irradiation almost no reduction products are detected over Ru/HNT at ambient temperature. As light intensity increased from 0.64 to 2.05 W cm^{-2}, the yield of product CH_4 over Ru/HNT rises sharply and the CH_4 selectivity remains almost unchanged above 92%, with a small amount of CO production (Fig. 1b). With further increasing light intensity, the CH_4 selectivity of Ru/HNT decreases significantly at the light intensity of 2.86 and 3.19 W cm^{-2}, because of the occurrence of thermodynamically favorable reverse water-gas shift reaction at high temperatures [22]. Under 2.05 W cm^{-2} light irradiation, Ru/HNT exhibits the optimal photothermal catalytic performance, and corresponding yield for CH_4 is up to 1704 $mmolCH_4\ g_{cat}^{-1}\ h^{-1}$ with a selectivity of 93% and a CO_2 conversion rate of 68%.

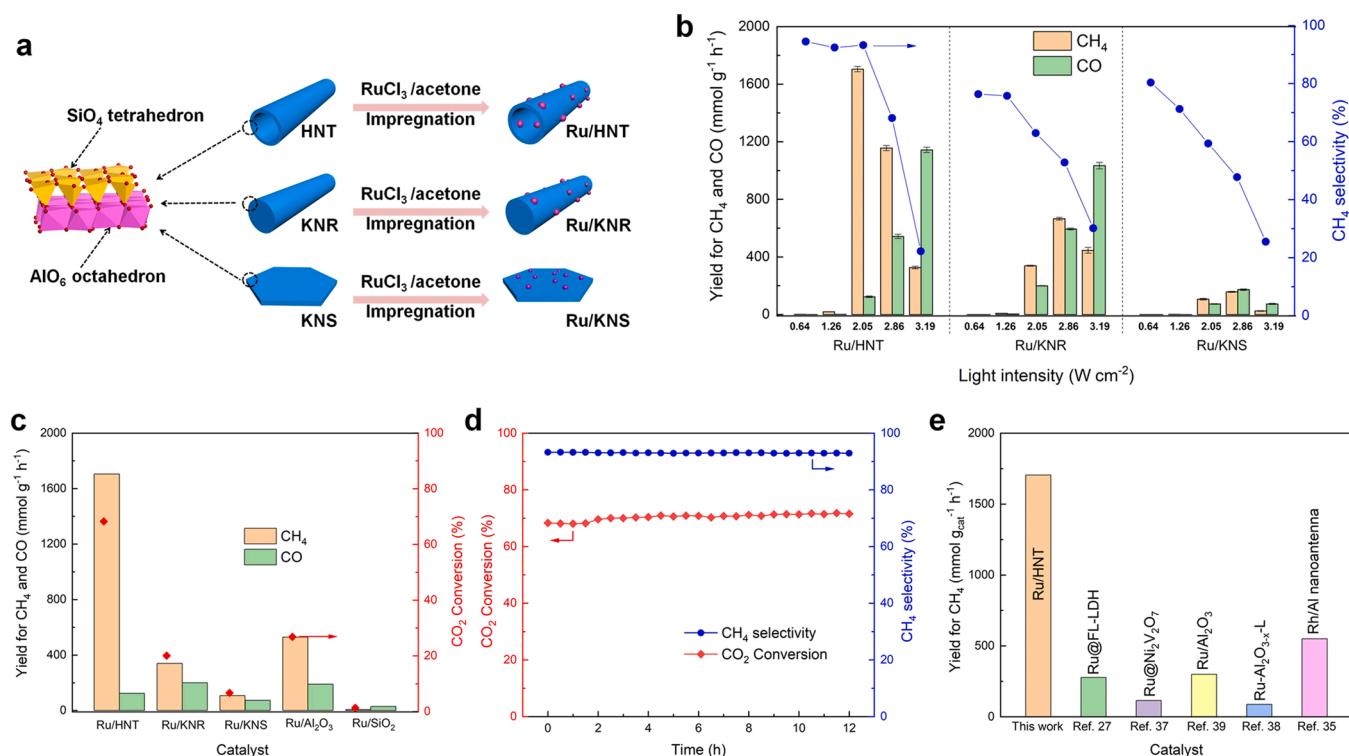Compared to Ru/HNT, both Ru/KNR and Ru/KNS show significantly

Fig. 1. Photothermal catalytic performance of Ru/HNT, Ru/KNR and Ru/KNS for CO_2 reduction. a) The preparation process of Ru/HNT, Ru/KNR and Ru/KNS. b) The yield for CH_4 and CO, and CH_4 selectivity of Ru/HNT, Ru/KNR and Ru/KNS under different light irradiation. c) The yield and CO_2 conversion of catalysts under 2.05 W cm^{-2} light irradiation. d) Continuous stability test of photothermal CO_2 reduction over Ru/HNT under 2.05 W cm^{-2} light irradiation for 12 h. e) Comparison of CH_4 yield in photothermal catalytic CO_2 reduction with other recently reported catalysts.

lower CH_4 yield and selectivity under the light irradiation with the same intensity. The CH_4 selectivities over Ru/KNR and Ru/KNS consistently decline with increasing light intensity, and they are all lower less than 80%. Particularly, the CO_2 conversion rate of Ru/HNT (68%) is greatly superior than that of Ru/KNR (20%) and Ru/KNS (7%) under 2.05 W cm^{-2} light irradiation (Fig. 1c), indicating that the hollow nanotube is beneficial for light absorption, reaction gas transmission and CO_2 methanation, while the two-dimensional kaolinite nanosheets are unfavorable for light transmittance and gas transmission. The above results indicate the tubular morphology exhibits obvious advantages as the support materials of Ru nanoparticles compared to clubbed and lamellar morphology in the photothermal catalytic CO_2 reduction.

In addition, we found that the photothermal CO_2 methanation performance of Ru/HNT is remarkably higher than that of commercial Al_2O_3 and SiO_2 supported Ru (Fig. 1c). The continuous stability test demonstrates that the CH_4 selectivity and CO_2 conversion over Ru/HNT under continuous flow conditions remain stable without obvious reduction during 12 h (Fig. 1d), revealing the high durability of Ru/HNT. More importantly, the photothermal CO_2 reduction performance of Ru/HNT is substantially superior to by far reported Ru-based and other metals catalysts [7,20,29–31,42–48] (Fig. 1e, Table S1). Considering the resource and cost advantages of halloysite, Ru/HNT might be a promising photothermal catalyst for large-scale CO_2 reduction application.

3.2. Characterizations of Ru/HNT

Microscopic images of HNT (Fig. S2) exhibit the morphology of hollow nanotube with clean internal and external surfaces. The micro morphology images of Ru/HNT show no obvious change compared to HNT, although the surface of Ru/HNT appears rougher due to the presence of Ru nanoparticles. The nanotubes are arranged into staggered clusters (Fig. 2a), which probably facilitates light absorption and gas

transmission. Ru nanoparticles are evenly assembled on the nanotubes (Fig. 2b-c), internal diameter of which is large enough for CO_2 and CH_4 molecules to pass through. From the high-resolution TEM (HRTEM) image of Ru/HNT (Fig. 2d), the lattice spacing of 0.205 nm identities with the (101) plane of Ru nanocrystals, and the sizes of Ru nanoparticles are distributed in 1–3.5 nm (Fig. S3). Ru/KNR and Ru/KNS show the similar particle size distribution of Ru nanoparticles (Fig. S4-S7). It is reported that the product selectivity of CO_2 reduction depends on the sizes of Ru clusters [22], and accordingly the majority of Ru nanocrystals in these three catalysts are active sites for CH_4 formation. The scanning TEM (STEM) and elemental mapping images of Ru/HNT (Fig. 2e-f) show that Ru element distribution coincides with Si and Al element, which reveals the uniform distribution of Ru nanoparticles on the HNT. The element content of Ru is approximately loading amount of 3 wt% from energy dispersive spectroscopy (EDS) analysis (Fig. S8). The microstructures and Ru nanoparticle sizes of Ru/HNT after stability test exhibit no significant change (Fig. S9), indicating the excellent structural stability of Ru/HNT.

The X-ray diffraction (XRD) pattern of Ru/HNT (Fig. 2g) is consistent with halloysite (JCPDS card NO. 29–1487). The diffraction peak of Ru is not detected, probably due to the low content, high dispersion and small size of Ru nanoparticles. Similar results are found on Ru/KNR and Ru/KNS, with the detection of only the diffraction peaks of kaolinite (Fig. S10). The N_2 adsorption/desorption isotherm curves of Ru/HNT (Fig. 2h) conform a type-IV isotherm, corresponding to mesoporous structure of nanotubes, and its Brunauer–Emmett–Teller (BET) specific surface area is 54.58 m^2 g^{-1}, which is much higher than that of Ru/KNR (14.52 m^2 g^{-1}) and Ru/KNS (18.77 m^2 g^{-1}) (Fig. S11-S12). The pore size distributions of Ru/HNT exhibit a bimodal porous structure with the size of 2–100 nm. The large surface area and appropriate pore structure of Ru/HNT could facilitate the transfer and adsorption of reactant gases, ultimately enhancing catalytic performance.

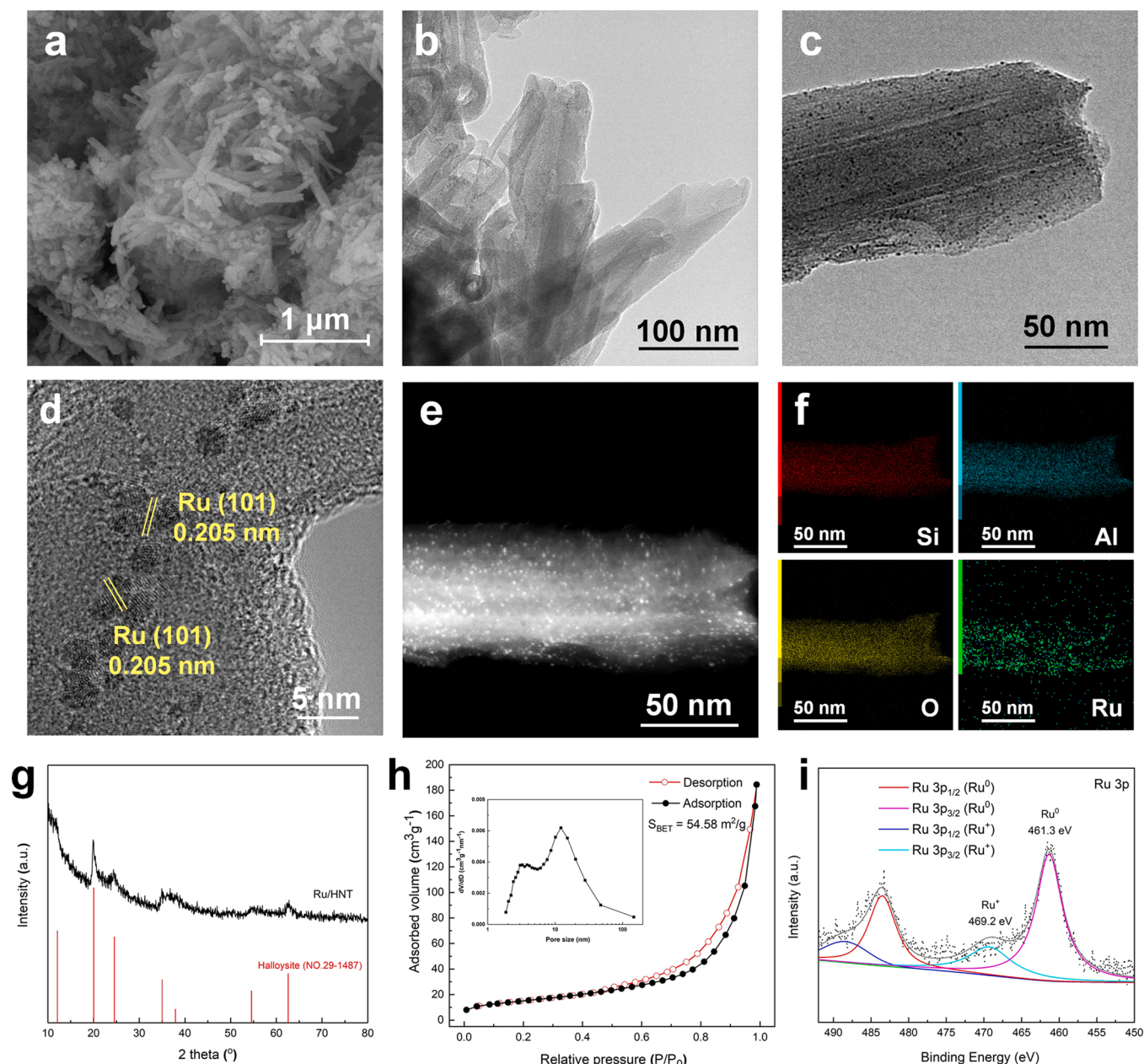The high-resolution scan X-ray photoelectron spectrum (XPS) for Ru

Fig. 2. Morphology and structure characterization of Ru/HNT. a) SEM image, b,c) TEM images, d) HRTEM image, e) STEM image and f) elemental mapping images of Ru/HNT. g) XRD pattern of Ru/HNT. h) N$_2$ adsorption/desorption isotherm curves and BJH pore size distributions of Ru/HNT. i) High-resolution scan XPS spectrum for Ru 3p of Ru/HNT.

3p of Ru/HNT (Fig. 2i) indicates the metallic Ru (Ru^0) with a small amount of oxidation state (Ru$^+$) [49], which is ascribed to formation of the Ru-O-SiO$_x$ and Ru-O-AlO$_x$ interfaces. Compared to Ru/KNR and Ru/KNS (Fig. 3a-b), Ru/HNT possesses more Ru oxidation state (Table S2), indicating more interfaces of Ru-O-SiO$_x$ and Ru-O-AlO$_x$ in Ru/HNT. Moreover, the peaks of Si 2p and Al 2p of Ru/HNT exhibit large shifts to higher binding energies after loading Ru (Fig. 3c-f), which may be due to more electron transfer from HNT to Ru, whereas no obvious shift is observed in Ru/KNR and Ru/KNS. This interfacial charge transport demonstrates the strong electronic interaction between Ru and HNT in Ru/HNT, and such strong interfacial interaction together with more interfaces of Ru-O-SiO$_x$ and Ru-O-AlO$_x$ are conducive for the improvement of photothermal catalytic performance [45,50,51].

The Fourier transform infrared (FTIR) spectra (Fig. S13) indicate that Ru/HNT, Ru/KNR and Ru/KNS possess abundant surface hydroxyl groups, which can adsorb CO$_2$ to form carbonate and formate. The H$_2$ temperature-programmed reduction curves of Ru/HNT, Ru/KNR and Ru/KNS (Fig. S14) exhibit distinct reduction peaks around 150 °C, attributed to the reduction of Ru oxide to Ru metal. The H$_2$ consumptions are higher than the nominal value for the reduction of Ru oxide own to H-spillover. The CO$_2$ temperature-programmed desorption (TPD) of catalyst was measured to evaluate the surface basic sites. From the CO$_2$ TPD curves (Fig. S15a), the desorption peak of Ru/HNT is higher owe to its more CO$_2$ adsorption sites, which is beneficial to enhance catalytic activity for CO$_2$ reduction. The CO$_2$ TPD curves of HNT, KNR and KNS (Fig. S15b) show only slight differences compared with that of Ru/HNT, Ru/KNR and Ru/KNS. The number and strength of the surface basic sites of support materials and Ru-loaded supports are similar, suggesting that support materials are CO$_2$ adsorption sites [18].
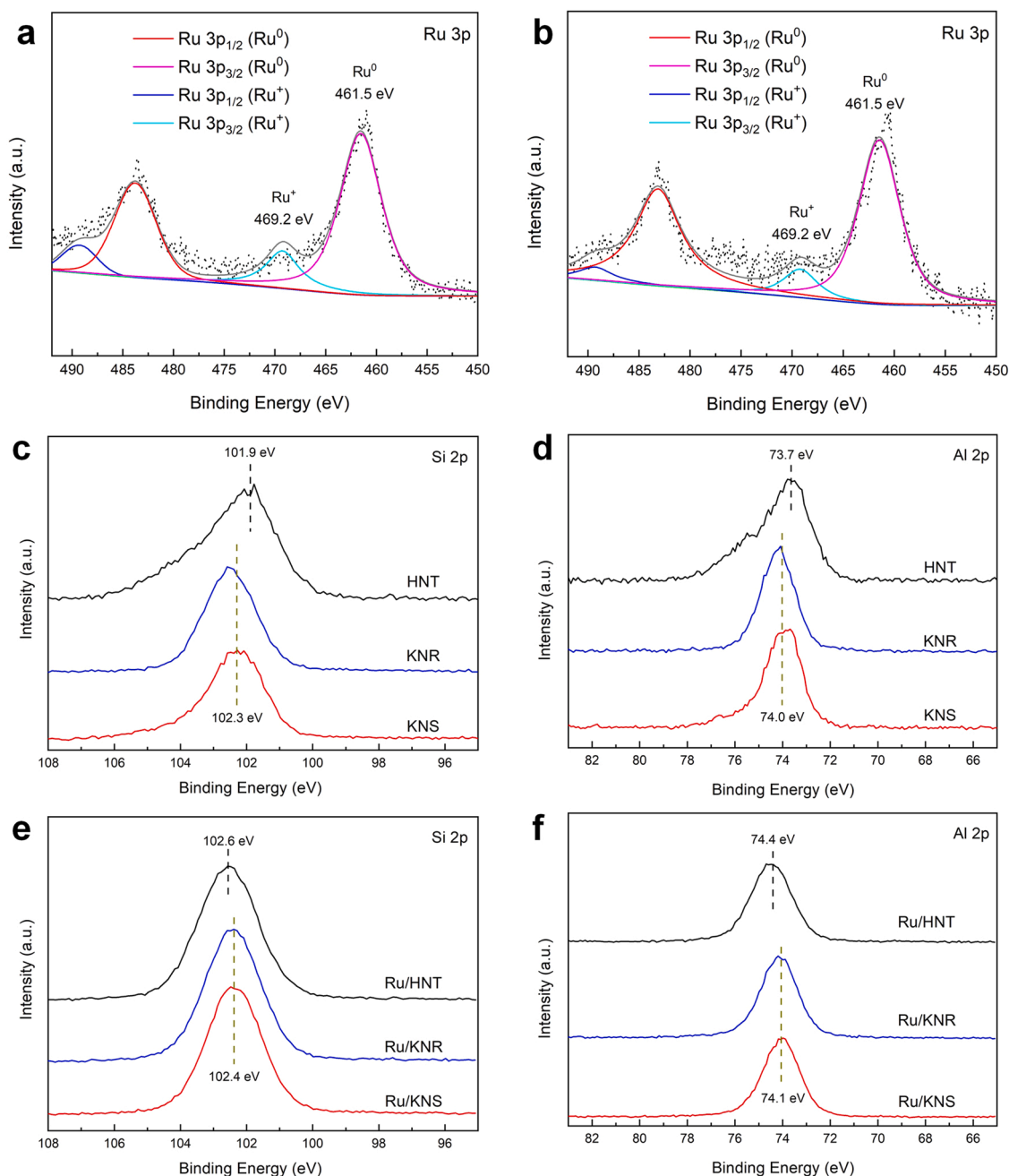
Fig. 3. Interfacial characterization of Ru/HNT, Ru/KNR and Ru/KNS. High-resolution scan XPS spectra for Ru 3p of a) Ru/KNR and b) Ru/KNS. High-resolution scan XPS spectra for c) Si 2p and d) Al 2p electrons of HNT, KNR and KNS. High-resolution scan XPS spectra for e) Si 2p and f) Al 2p electrons of Ru/HNT, Ru/KNR and Ru/KNS.

3.3. Mechanism investigation of photothermal catalytic CO_2 reduction

The ultraviolet-visible-near infrared (UV–vis–NIR) absorption spectra (Fig. 4b) show that Ru/HNT exhibits the highest light absorption property from the UV to IR light range compared to Ru/KNR and Ru/KNS, which might be attributed to multiple reflection and absorption of light in one-dimensional hollow nanotubes (Fig. 4a) [29]. Besides, Ru/HNT possesses higher thermal conductivity than Ru/KNR and Ru/KNS (Fig. S16), due to the stronger convective heat transfer of nanotubes. High light absorption and thermal conductivity lead to increased light energy utilization and enhanced photothermal effect [52]. It is well-known that Ru nanoparticles can act as a "nanoheater" [44] to increase the surface temperature of catalyst via photothermal effect, which contributes to efficient photothermal catalysis and light energy utilization.

As a result, the temperatures of the catalysts measured by a thermocouple rise rapidly under light irradiation, maintaining equilibrium after 10 min (Fig. 4c, Fig. S17-S18), and Ru/HNT possesses highest equilibrium temperature than Ru/KNR and Ru/KNS at various light intensity (Fig. 4d), thereby resulting in the best photothermal CO_2 reduction performance on Ru/HNT. For instance, under 2.05 W cm^{-2} light irradiation, the equilibrium temperatures of Ru/HNT, Ru/KNR and Ru/KNS is 327 °C, 318 °C and 272 °C, respectively. The equilibrium temperatures of Ru/HNT and Ru/KNR are higher than that of Ru/KNS, suggesting that one-dimensional nanotubes and nanorods are more conducive to light transmission and absorption compared to two-dimensional nanosheets [53]. The equilibrium temperatures of HNT, KNR, KNS without Ru are all below 150 °C (Fig. S19) under different
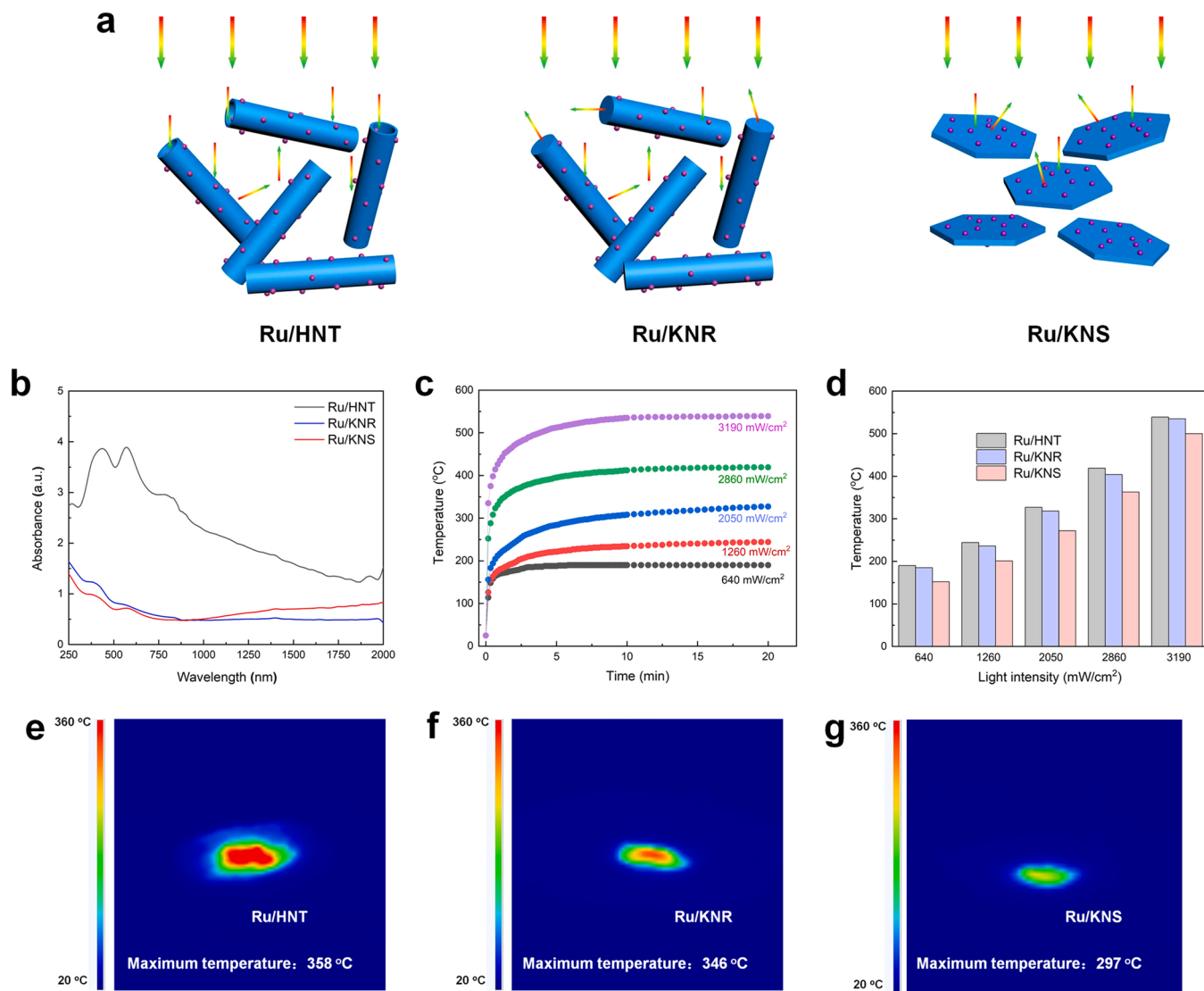
Fig. 4. Photothermal property of Ru/HNT, Ru/KNR and Ru/KNS. a) Schematic illustration of light absorption process of Ru/HNT, Ru/KNR and Ru/KNS. b) UV–vis–NIR absorption spectra of Ru/HNT, Ru/KNR and Ru/KNS. c) The temperature variation of Ru/HNT irradiated for 20 min d) The equilibrium temperature of Ru/HNT, Ru/KNR, Ru/KNS irradiated after 20 min. The infrared images of e) Ru/HNT, f) Ru/KNR and g) Ru/KNS under 2.05 W cm^{-2} light irradiation after 20 min.
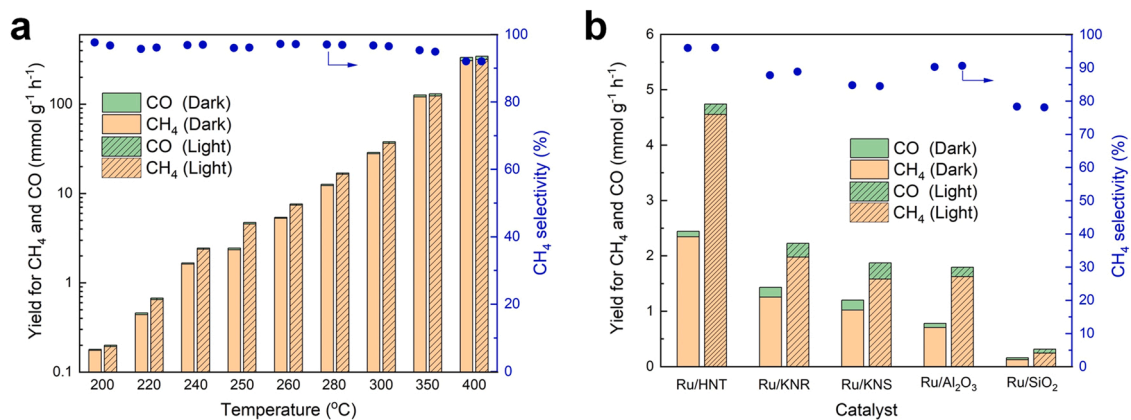

Fig. 5. Photo-assisted thermocatalytic performance of Ru/HNT. a) Photo-assisted thermocatalytic yield for CH$_4$ and CO, and CH$_4$ selectivity of Ru/HNT at different temperatures. b) Photo-assisted thermocatalytic yield for CH$_4$ and CO, and CH$_4$ selectivity of Ru/HNT, Ru/KNR, Ru/KNS, Ru/Al$_2$O$_3$ and Ru/SiO$_2$ at 250 °C.

light intensity irradiation, much lower than those of catalysts with Ru, which proves the crucial effect of Ru as a nanoheater on the the photothermal conversion.

The temperature distribution of catalyst surface was monitored with an infrared thermograph, and the sample surface was at room temperature before irradiation (Fig. S20). The surface temperature of Ru/HNT responds rapidly to light irradiation (Fig. S21), which is beneficial for the control of photothermal catalytic reactions [54]. From the infrared images (Fig. 4e-g), the temperature distributions of catalyst surfaces are relatively concentrated and significantly higher than the ambient temperature. It is noted that the temperatures measured by infrared thermograph are slightly higher than that by thermocouple, which might be due to difference of measurement methods and areas.

In addition to photothermal effect, the photo enhancement effect derived from hot carrier-activated reactants possibly facilitates catalytic activity in photothermal reactions [55]. To study this effect, we conducted the photo-assisted thermocatalytic CO_2 reduction in a continuous flow reactor (Fig. S22) under visible light irradiation (0.58 W cm^{-2}) [56–58] The yield of CH_4 increases drastically as the temperature rises on Ru/HNT without light irradiation, with a slight downward trend in CH_4 selectivity (Fig. 5a). Under light irradiation, an obvious enhanced CH_4 and CO yield is observed at temperatures below 300 °C with almost no enhancement above 300 °C, whereas illumination has little effect on CH_4 selectivity. We speculate that the observed photo enhancement at low temperatures (<300 °C) is mainly derived from the photo-induced thermal effect and/or hot electrons-CO_2 activation [59] due to the formation of hybrid orbitals between Ru and CO_2 [54].

The photo enhancement ratio, defined as the ratio of the yield increments under light irradiated to yield in thermal catalysis, increases first and then decreases with increasing the reaction temperature on Ru/HNT [60], and it is the highest up to 94% at 250 °C. Moreover, the photo enhancement ratio of Ru/HNT is obviously higher than that of Ru/KNR, Ru/KNS, Ru/Al$_2$O$_3$ and Ru/SiO$_2$(Fig. 5b), which is consistent with the superior photothermal catalytic ability of Ru/HNT. In addition, when the Ru loading amounts on HNT increases from 1% to 3%, the photo enhancement ratio and CH_4 selectivity increase sharply (Fig. S23-S24), suggesting the critical roles of Ru nanoparticles as the "nanoheater" and catalytical active site for CO_2 methanation. Further increasing Ru loading amounts leads to a slow increase in the catalytic performance.

The photothermal catalytic CH_4 yield of Ru/HNT (327 °C) under 2.05 W cm^{-2} light irradiation is even superior than that of Ru/KNR (404 °C) and Ru/KNS (363 °C) under 2.86 W cm^{-2} light irradiation, demonstrating that the intrinsic catalytic ability of Ru/HNT plays a crucial part in addition to excellent photothermal capabilities. The intrinsic catalytic ability probably results from the unique surface chemical compositions and structures of HNT. To investigate their effect on catalytic activity, the surface properties of HNT were adjusted by facile acid and alkali treatments. Acid treatments could remove the partial aluminum oxide on the HNT surface (HNT-Acid), resulting in silicon-rich surfaces, while alkali treatments could remove both the partial silicon oxide and aluminum oxide (HNT-Alkali) [61,62]. Ru nanoparticles were supported on HNT-Acid and HNT-Alkali via the similar wet impregnation (Fig. 6a). The oxide support material usually provides sites for CO_2 adsorption in the Ru-supported catalysts. From Fig. 6b, Ru/HNT possesses a large amount of basic sites with CO_2 desorption at 476 °C (3.21 mmol g^{-1}), higher than the common basic support (Ru/CeO$_2$, 1.25 mmol g^{-1}) [18]. Compared to Ru/HNT, HNT-Acid contains similar strength but with less amount of surface basic sites. This result reveals that acid treatment reduces surface sites for CO_2 adsorption, which is unfavorable for catalytic CO_2 reduction. HNT-Alkali possesses stronger surface basic sites with CO_2 desorption peak at 543 °C.
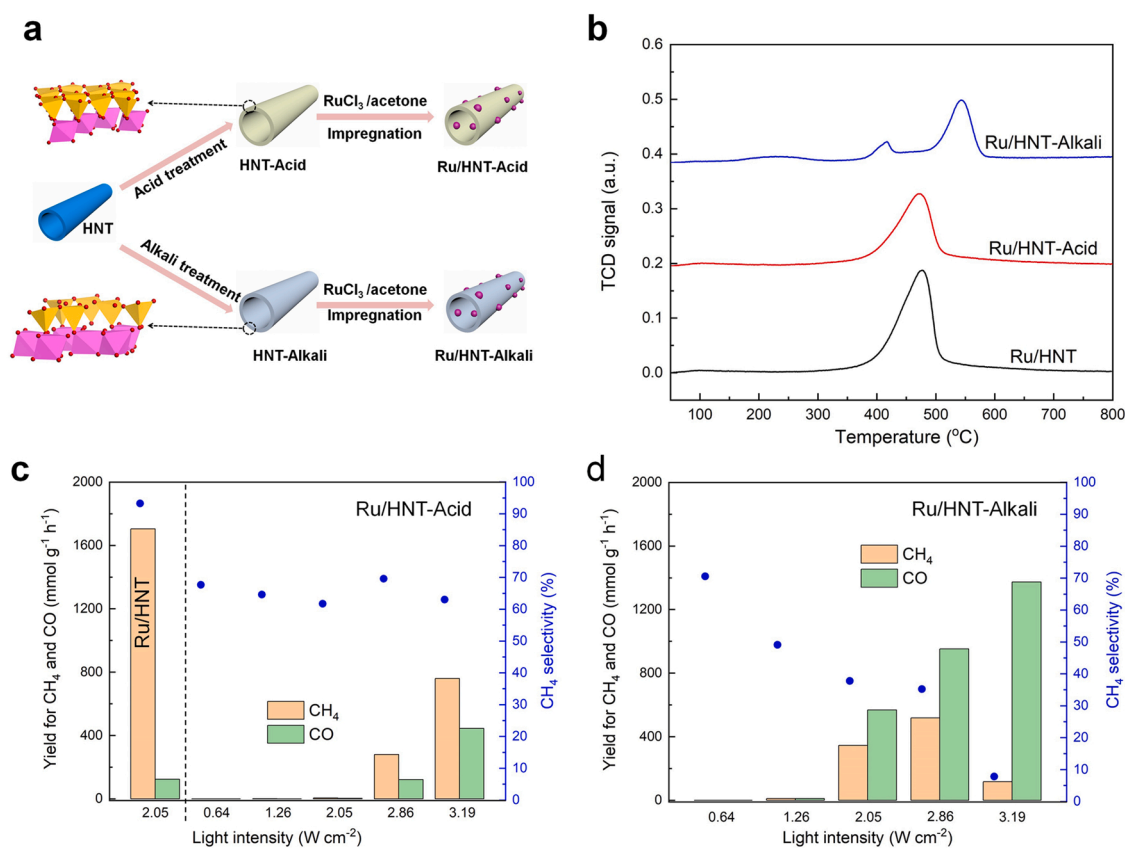

Fig. 6. Photothermal catalytic performance of Ru/HNT with acid and alkali treatments. a) the synthesis process of Ru/HNT-Acid and Ru/HNT-Alkali. b) CO_2 TPD curves of Ru/HNT, Ru/HNT-Acid and Ru/HNT-Alkali. Photothermal catalytic yield for CH_4 and CO, and CH_4 selectivity of c) Ru/HNT-Acid (the first column for Ru/HNT as a comparison) and d) Ru/HNT-Alkali.

Ru/HNT-Acid exhibits lower catalytic activity (Fig. 6c), which might be attributed to the poor CO_2 adsorption capacity. The Ru supported on HNT-Alkali (Ru/HNT-Alkali) possesses high CO selectivity (92%) with light intensity of 3.19 W cm^{-2} due to the occurrence of reverse water-gas shift reaction [22] (Fig. 6d). According to DFT calculations, the adsorption energy of *CO on the HNT-Alkali (0.25 eV) is far weaker than that of HNT (−1.58 eV) (Table S3), indicating that *CO would easily desorb from the HNT-Alkali surface to promote reverse water-gas shift reaction. In addition, *COH as the following intermediate for methanation is not stable on HNT-Alkali surface (Fig. S25), and the calculations demonstrate that *COOH is formed due to the assistance of a neighboring O atom. These suggest that the Ru/HNT-Alkali could present lower CH_4 selectivity than the Ru/HNT. The special Si-Al-O structures and abundant hydroxyl groups of the HNT surfaces are conducive to the chemical adsorption and activation of CO_2, and Ru nanoparticles could facilitate the activation of H_2 and the hydrogenation of CO_2 [29]. These results indicate the excellent photothermal CO_2 methanation performance of Ru/HNT could benefit from special and whole surface properties of HNT.

In situ diffuse reflectance infrared Fourier transform spectroscopy (DRIFTS) measurements were performed to explore the mechanism of photothermal CO_2 methanation. The in situ DRIFTS spectra of Ru/HNT at different temperatures (Fig. 7a) were recorded after reaction equilibrium under the same continuous flow reaction conditions as thermal catalysis. The signals of characteristic peaks increase sharply with increasing the reaction temperature. The bands at 3680, 3637 and 1795 cm^{-1} could be attributed to the H-O-H stretching vibration of generated gaseous water, and the bands at 3015 cm^{-1} corresponds to the CH_4 gas as the CO_2 reduction product [18,63,64]. The bands at 1507 and 2723 cm^{-1} could be credited to the carbonate and formate species,

indicating the formate pathway of photothermal CO_2 reduction over Ru/HNT [25,65,66]. The in situ DRIFTS spectra of Ru/HNT at 250 °C and 400 °C (Fig. 7b,c) were further recorded in a batch reactor. The peaks of water, CH_4 and formate species gradually become stronger with the prolonged reaction time. In addition, the peak intensities grow faster at 400 °C, indicative of the higher reaction rate. To investigate the effect of illumination on the intermediates, the in situ DRIFTS spectra of Ru/HNT with or without light radiation were recorded under a continuous flow reaction conditions at 250 °C(Fig. 7d). The peaks of CH_4 and formate species are enhanced obviously after light irradiation, indicating that light could promote CO_2 methanation at appropriate reaction temperatures.

Based on the above discussion, photothermal catalytic reaction mechanism for CO_2 reduction over Ru/HNT is proposed through the formate pathway as shown in Fig. 8. Ru nanoparticles act as "nano-heater" to convert light energy into heat energy via photothermal effect under irradiation, thereby triggering catalytic CO_2 methanation reaction. Via the chemisorption on Ru nanoparticles, H_2 is dissociated into H adatoms, which are then spilled to the surface of HNT for CO_2 reduction. Molecular CO_2 adsorbed on HNT is first reduced to *CO_2H species [44]. The *CO_2H intermediate is further reduced and dissociated in to H_2O and *CO, minor amounts of which were desorbed to form CO by a reverse water-gas shift reaction pathway [67]. While the large amount of *CO species are subsequently hydrogenated to form *COH, *CH_2 *O and *CH_3 intermediates in turn [68], as evidenced by the results of DRIFTS spectra, and eventually converted into CH_4 by methanation reaction.
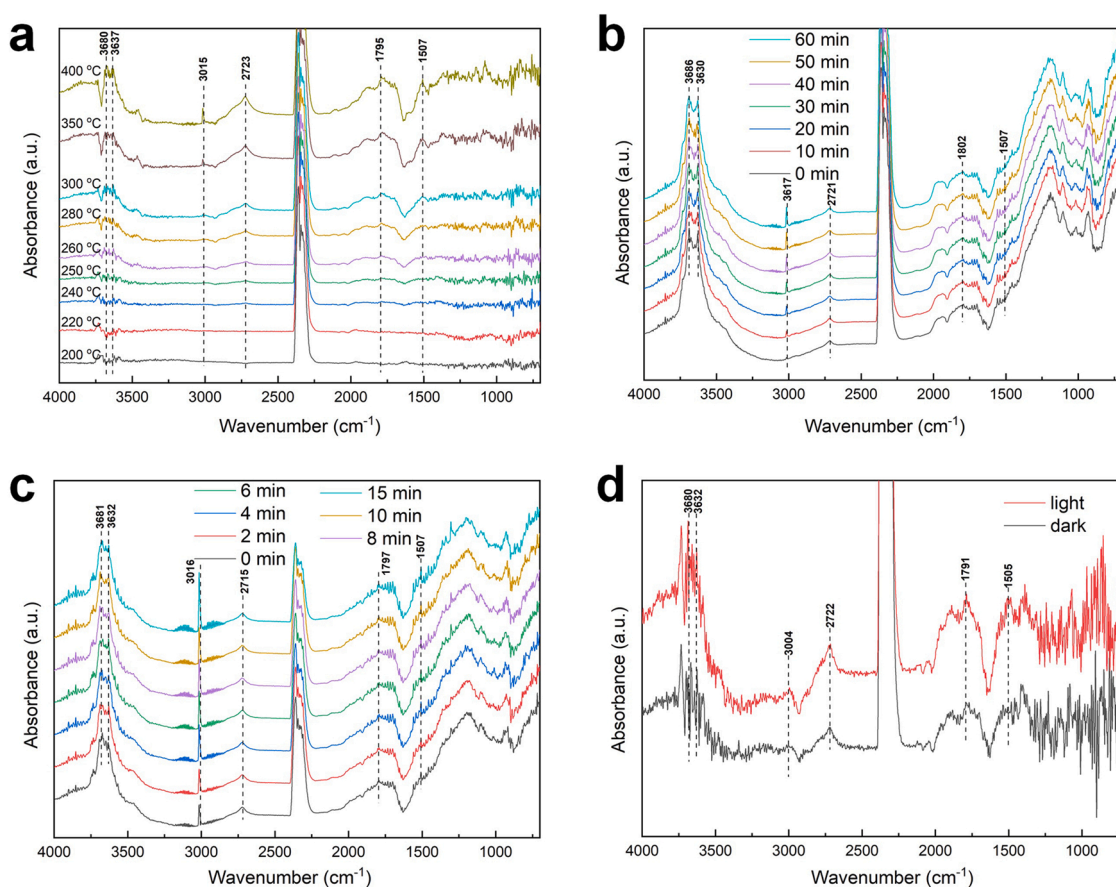

Fig. 7. In situ DRIFTS spectra of Ru/HNT. a) In situ DRIFTS spectra of Ru/HNT at different temperature in a flow reactor. In situ DRIFTS spectra of Ru/HNT at b) 250 °C and c) 400 °C in a batch reactor. d) In situ DRIFTS spectra of Ru/HNT with or without light radiation at 250 °C in a flow reactor.
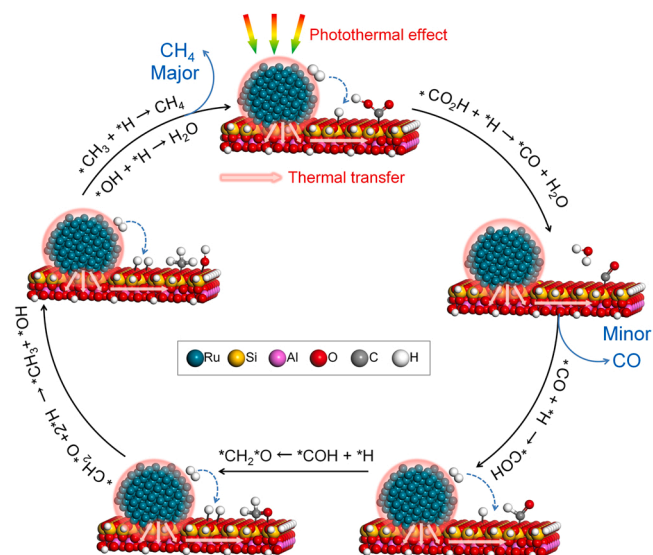
Fig. 8. Proposed photothermal catalytic reaction mechanism for CO_2 reduction over Ru/HNT.

4. Conclusion

Ru/HNT prepared by a facile wet impregnation method boosts the outstanding photothermal catalytic activity and selectivity of CO_2 methanation under continuous flow conditions. The optimized catalytic performance is up to 1704 mmolCH_4 g_{cat}^{-1} h^{-1} with 93% CH_4 selectivity and 68% CO_2 conversion, surpassing any other Ru-based catalysts in photothermal CO_2 reduction. It could be attributed to unique mesoporous tubular structure, excellent ability of light-to-heat and interfacial interactions between HNT and Ru. The photothermal catalytic performance depends sensitively on the surface properties of nanotubes, which could be tuned via facile surface acid-alkali treatments. The special surface properties of Ru/HNT are conducive to adsorption and activation of CO_2 and H_2, and the reaction mechanism of photothermal CO_2 methanation is a formate pathway. This study provides a guideline to design support materials for photothermal catalyst of CO_2 reduction under continuous flow conditions.

CRediT authorship contribution statement

Kang Peng: Conceptualization, Methodology, Investigation, Data curation, Writing – original draft, Funding acquisition. **Jingying Ye:** Methodology, Validation. **Hongjie Wang**: Conceptualization Writing – review & editing, Funding acquisition. **Hui Song**: Conceptualization, Methodology, Writing – review & editing. **Bowen Deng**: Methodology, Validation. **Shuang Song**: Methodology, Validation. **Yihan Wang**: Validation. **Linjie Zuo:** Validation. **Jinhua Ye:** Conceptualization, Writing – review & editing, Supervision, Validation, Funding acquisition.

Declaration of Competing Interest

The authors declare that they have no known competing financial interests or personal relationships that could have appeared to influence the work reported in this paper.

Data availability

Data will be made available on request.

Appendix A. Supporting information

Supplementary data associated with this article can be found in the online version at doi:10.1016/j.apcatb.2022.122262.

References

[1] W. Gao, S. Liang, R. Wang, Q. Jiang, Y. Zhang, Q. Zheng, B. Xie, C.Y. Toe, X. Zhu, J. Wang, L. Huang, Y. Gao, Z. Wang, C. Jo, Q. Wang, L. Wang, Y. Liu, B. Louis, J. Scott, A.C. Roger, R. Amal, H. He, S.E. Park, Industrial carbon dioxide capture and utilization: State of the art and future challenges, Chem. Soc. Rev. 49 (2020) 8584–8686.

[2] H. Seo, M. Rahimi, T.A. Hatton, Electrochemical carbon dioxide capture and release with a redox-active amine, J. Am. Chem. Soc. 144 (2022) 2164–2170.

[3] N.N. Vu, S. Kaliaguine, T.O. Do, Critical aspects and recent advances in structural engineering of photocatalysts for sunlight-driven photocatalytic reduction of CO_2 into fuels, Adv. Funct. Mater. 29 (2019) 1901825.

[4] S.F. Hung, A. Xu, X. Wang, F. Li, S.H. Hsu, Y. Li, J. Wicks, E.G. Cervantes, A. S. Rasouli, Y.C. Li, M. Luo, D.H. Nam, N. Wang, T. Peng, Y. Yan, G. Lee, E. H. Sargent, A metal-supported single-atom catalytic site enables carbon dioxide hydrogenation, Nat. Commun. 13 (2022) 819.

[5] I. Sullivan, A. Goryachev, I.A. Digdaya, X. Li, H.A. Atwater, D.A. Vermaas, C. Xiang, Coupling electrochemical CO_2 conversion with CO_2 capture, Nat. Catal. 4 (2021) 952–958.

[6] U. Ulmer, T. Dingle, P.N. Duchesne, R.H. Morris, A. Tavasoli, T. Wood, G.A. Ozin, Fundamentals and applications of photocatalytic CO_2 methanation, Nat. Commun. 10 (2019) 2005–2008.

[7] M. Cai, Z. Wu, Z. Li, L. Wang, W. Sun, A.A. Tountas, C. Li, S. Wang, K. Feng, A. B. Xu, S. Tang, A. Tavasoli, M. Peng, W. Liu, A.S. Helmy, L. He, G.A. Ozin, X. Zhang, Greenhouse-inspired supra-photothermal CO_2 catalysis, Nat. Energy 6 (2021) 807–814.

[8] X. Yan, W. Sun, L. Fan, P.N. Duchesne, W. Wang, C. Kübel, D. Wang, S.G.H. Kumar, Y.F. Li, A. Tavasoli, T.E. Wood, D.L.H. Hung, L. Wan, L. Wang, R. Song, J. Guo, I. Gourevich, A.A. Jelle, J. Lu, R. Li, B.D. Hatton, G.A. Ozin, Nickel@siloxene catalytic nanosheets for high-performance CO_2 methanation, Nat. Commun. 10 (2019) 2005–2008.

[9] Z. Wang, H. Song, H. Liu, J. Ye, Coupling of solar energy and thermal energy for carbon dioxide reduction: status and prospects, Angew. Chem. -Int. Ed. 132 (2020) 8092–8111.

[10] L. Zhou, D.F. Swearer, C. Zhang, H. Robatjazi, H. Zhao, L. Henderson, L. Dong, P. Christopher, E.A. Carter, P. Nordlander, N.J. Halas, Quantifying hot carrier and thermal contributions in plasmonic photocatalysis, Science 362 (2018) 69–72.

[11] Z. Zhang, C. Mao, D.M. Meira, P.N. Duchesne, A.A. Tountas, Z. Li, C. Qiu, S. Tang, R. Song, X. Ding, J. Sun, J. Yu, J.Y. Howe, W. Tu, L. Wang, G.A. Ozin, New black indium oxide-tandem photothermal CO_2-H_2 methanol selective catalyst, Nat. Commun. 13 (2022) 1512.

[12] H. Lin, S. Luo, H. Zhang, J. Ye, Toward solar-driven carbon recycling, Joule 6 (2022) 294–314.

[13] M. Ghoussoub, M. Xia, P.N. Duchesne, D. Segal, G. Ozin, Principles of photothermal gas-phase heterogeneous CO_2 catalysis, Energy Environ. Sci. 12 (2019) 1122–1142.

[14] D. Mateo, J.L. Cerrillo, S. Durini, J. Gascon, Fundamentals and applications of photo-thermal catalysis, Chem. Soc. Rev. 50 (2021) 2173–2210.

[15] J. Hong, C. Xu, B. Deng, Y. Gao, X. Zhu, X. Zhang, Y. Zhang, Photothermal chemistry based on solar energy: from synergistic effects to practical applications, Adv. Sci. (2021) 2103926.

[16] B. Deng, H. Song, K. Peng, Q. Li, J. Ye, Metal-organic framework-derived Ga-Cu/CeO_2 catalyst for highly efficient photothermal catalytic CO_2 reduction, Appl. Catal. B-Environ. 298 (2021), 120519.

[17] N. Keller, J. Ivanez, J. Highfield, A.M. Ruppert, Photo-/thermal synergies in heterogeneous catalysis: towards low-temperature (solar-driven) processing for sustainable energy and chemicals, Appl. Catal. B-Environ. 296 (2021), 120320.

[18] J.A.H. Dreyer, P. Li, L. Zhang, G.K. Beh, R. Zhang, P.H.L. Sit, W.Y. Teoh, Influence of the oxide support reducibility on the CO_2 methanation over Ru-based catalysts, Appl. Catal. B-Environ. 219 (2017) 715–726.

[19] H. Huang, Q. Dai, X. Wang, Morphology effect of Ru/CeO_2 catalysts for the catalytic combustion of chlorobenzene, Appl. Catal. B-Environ. 158- 159 (2014) 96–105.

[20] P.G. O'Brien, A. Sandhel, T.E. Wood, A.A. Jelle, L.B. Hoch, D.D. Perovic, C. A. Mims, G.A. Ozin, Photomethanation of gaseous CO_2 over Ru/silicon nanowire catalysts with visible and near-infrared photons, Adv. Sci. 1 (2014) 1400001.

[21] A. Bermejo-López, B. Pereda-Ayo, J.A. González-Marcos, J.R. González-Velasco, Mechanism of the CO₂ storage and in situ hydrogenation to CH₄. Temperature and adsorbent loading effects over Ru-CaO/Al₂O₃ and Ru-Na₂CO₃/Al₂O₃ catalysts, Appl. Catal. B-Environ. 256 (2019), 117845.

[22] J.H. Kwak, L. Kovarik, J. Szanyi, CO₂ reduction on supported Ru/Al₂O₃ catalysts: cluster size dependence of product selectivity, ACS Catal. 3 (2013) 2449–2455.

[23] X. Meng, T. Wang, L. Liu, S. Ouyang, P. Li, H. Hu, T. Kako, H. Iwai, A. Tanaka, J. Ye, Photothermal conversion of CO₂ into CH₄ with H₂ over group VIII nanocatalysts: An alternative approach for solar fuel production, Angew. Chem. -Int. Ed. 53 (2014) 11478–11482.

[24] A. Aitbekova, L. Wu, C.J. Wrasman, A. Boubnov, A.S. Hoffman, E.D. Goodman, S. R. Bare, M. Cargnello, Low-temperature restructuring of CeO₂-supported Ru nanoparticles determines selectivity in CO₂ catalytic reduction, J. Am. Chem. Soc. 140 (2018) 13736–13745.

[25] F. Wang, S. He, H. Chen, B. Wang, L. Zheng, M. Wei, D.G. Evans, X. Duan, Active site dependent reaction mechanism over Ru/CeO₂ catalyst toward CO₂ methanation, J. Am. Chem. Soc. 138 (2016) 6298–6305.

[26] M. Fan, J.D. Jimenez, S.N. Shirodkar, J. Wu, S. Chen, L. Song, M.M. Royko, J. Zhang, H. Guo, J. Cui, K. Zuo, W. Wang, C. Zhang, F. Yuan, R. Vajtai, J. Qian, J. Yang, B.I. Yakobson, J.M. Tour, J. Lauterbach, D. Sun, P.M. Ajayan, Atomic Ru immobilized on porous h-BN through simple vacuum filtration for highly active and selective CO₂ methanation, ACS Catal. 9 (2019) 10077–10086.

[27] A.M. Abdel-Mageed, D. Widmann, S.E. Olesen, I. Chorkendorff, J. Biskupek, R. J. Behm, Selective CO methanation on Ru/TiO₂ catalysts: Role and influence of metal–support interactions, ACS Catal. 5 (2015) 6753–6763.

[28] A. Kim, D.P. Debecker, F. Devred, V. Dubois, C. Sanchez, C. Sassoye, CO₂ methanation on Ru/TiO₂ catalysts: on the effect of mixing anatase and rutile TiO₂ supports, Appl. Catal. B-Environ. 220 (2018) 615–625.

[29] J. Ren, S. Ouyang, H. Xu, X. Meng, T. Wang, D. Wang, J. Ye, Targeting activation of CO₂ and H₂ over Ru-loaded ultrathin layered double hydroxides to achieve efficient photothermal CO₂ methanation in flow-type system, Adv. Energy Mater. 7 (2017) 1601657.

[30] A.A. Jelle, K.K. Ghuman, P.G. O'Brien, M. Hmadeh, A. Sandhel, D.D. Perovic, C. V. Singh, C.A. Mims, G.A. Ozin, Highly efficient ambient temperature CO₂ photomethanation catalyzed by nanostructured RuO₂ on silicon photonic crystal support, Adv. Energy Mater. 8 (2018) 1702277.

[31] P.G. O'Brien, K.K. Ghuman, A.A. Jelle, A. Sandhel, T.E. Wood, J.Y.Y. Loh, J. Jia, D. Perovic, C.V. Singh, N.P. Kherani, C.A. Mims, G.A. Ozin, Enhanced photothermal reduction of gaseous CO₂ over silicon photonic crystal supported ruthenium at ambient temperature, Energy Environ. Sci. 11 (2018) 3443–3451.

[32] K. Li, W. Zhou, X. Li, Q. Li, S.A.C. Carabineiro, S. Zhang, J. Fan, K. Lv, Synergistic effect of cyano defects and CaCO₃ in graphitic carbon nitride nanosheets for efficient visible-light-driven photocatalytic NO removal, J. Hazard. Mater. 442 (2023), 130040.

[33] N. Kang, W. Zhou, Z. Qi, Y. Li, Z. Wang, Q. Li, K. Lv, Recent progress of natural mineral materials in environmental remediation, Catalysts 12 (2022) 996.

[34] A. Glotov, A. Vutolkina, A. Pimerzin, V. Vinokurov, Y. Lvov, Clay nanotube-metal core/shell catalysts for hydroprocesses, Chem. Soc. Rev. 50 (2021) 9240–9277.

[35] M. Karolina Pierchala, F.B. Kadumudi, M. Mehrali, T.G. Zsurzsan, P.J. Kempen, M. P. Serdeczny, J. Spangenberg, T.L. Andresen, A. Dolatshahi-Pirouz, Soft electronic materials with combinatorial properties generated via mussel-inspired chemistry and halloysite nanotube reinforcement, ACS Nano 15 (2021) 9531–9549.

[36] S. Zhao, Y. Yuan, Q. Yu, B. Niu, J. Liao, Z. Guo, N. Wang, A dual-surface amidoximated halloysite nanotube for high-efficiency economical uranium extraction from seawater, Angew. Chem. -Int. Ed. 58 (2019) 14979–14985.

[37] X. Feng, D. Liu, B. Yan, M. Shao, Z. Hao, G. Yuan, H. Yu, Y. Zhang, Highly active PdO/Mn₃O₄/CeO₂ nanocomposites supported on one dimensional halloysite nanotubes for photoassisted thermal catalytic methane combustion, Angew. Chem. -Int. Ed. 60 (2021) 18552–18556.

[38] X. Li, R. Li, K. Peng, L. Fu, K. Zhao, H. Li, J. Peng, L. Wang, Interlayer functionalization of vermiculite derived silica with hierarchical layered porous structure for stable CO₂ adsorption, Chem. Eng. J. 435 (2022), 134875.

[39] K. Peng, P. Wan, H. Wang, L. Zuo, M. Niu, L. Su, L. Zhuang, X. Li, Unraveling the morphology effect of kandite MoS₂ nanosheets for enhancing electrocatalytic hydrogen evolution, Appl. Clay Sci. 212 (2021) 106211.

[40] G. Kresse, J. Furthmuller, Efficient iterative schemes for Ab initio total-energy calculations using a plane-wave basis set, Phys. Rev. B 54 (1996) 11169–11186.

[41] J.P. Perdew, K. Burke, M. Ernzerhof, Generalized gradient approximation made simple, Phys. Rev. Lett. 77 (1996) 3865–3868.

[42] G. Fu, M. Jiang, J. Liu, K. Zhang, Y. Hu, Y. Xiong, A. Tao, Z. Tie, Z. Jin, Rh/Al nanoantenna photothermal catalyst for wide-spectrum solar-driven CO₂ methanation with nearly 100% selectivity, Nano Lett. 21 (2021) 8824–8830.

[43] J. Jia, H. Wang, Z. Lu, P.G. O'Brien, M. Ghoussoub, P. Duchesne, Z. Zheng, P. Li, Q. Qiao, L. Wang, A. Gu, A.A. Jelle, Y. Dong, Q. Wang, K.K. Ghuman, T. Wood, C. Qian, Y. Shao, C. Qiu, M. Ye, Y. Zhu, Z.H. Lu, P. Zhang, A.S. Helmy, C.V. Singh, N.P. Kherani, D.D. Perovic, G.A. Ozin, Photothermal catalyst engineering: hydrogenation of gaseous CO₂ with high activity and tailored selectivity, Adv. Sci. 4 (2017) 1700252.

[44] Y. Chen, Y. Zhang, G. Fan, L. Song, G. Jia, H. Huang, S. Ouyang, J. Ye, Z. Li, Z. Zou, Cooperative catalysis coupling photo-/photothermal effect to drive Sabatier reaction with unprecedented conversion and selectivity, Joule 5 (2021) 3235–3251.

[45] X. Liu, C. Xing, F. Yang, Z. Liu, Y. Wang, T. Dong, L. Zhao, H. Liu, W. Zhou, Strong interaction over Ru/defects-rich aluminium oxide boosts photothermal CO₂ methanation via microchannel flow-type system, Adv. Energy Mater. 12 (2022) 2201009.

[46] R. Grote, R. Habets, J. Rohlfs, F. Sastre, N. Meulendijks, M. Xu, M.A. Verheijen, K. Elen, A. Hardy, M.K. Van Bael, T. den Hartog, P. Buskens, S, Information, Collective photothermal effect of Al₂O₃-supported spheroidal plasmonic Ru nanoparticle catalysts in the sunlight-powered Sabatier reaction, ChemCatChem 12 (2020) 5618–5622.

[47] D. Mateo, J. Albero, H. García, Titanium-perovskite-supported RuO₂ nanoparticles for photocatalytic CO₂ methanation, Joule 3 (2019) 1949–1962.

[48] Z. Wu, C. Li, Z. Li, K. Feng, M. Cai, D. Zhang, S. Wang, M. Chu, C. Zhang, J. Shen, Z. Huang, Y. Xiao, A. Ozin, X. Zhang, Niobium and titanium carbides (Mxenes) as photocatalysis superior photothermal supports for CO₂ photocatalysis, ACS Nano 15 (2021) 5696–5705.

[49] S. Zhu, X. Qin, F. Xiao, S. Yang, Y. Xu, Z. Tan, J. Li, J. Yan, Q. Chen, M. Chen, M. Shao, The role of ruthenium in improving the kinetics of hydrogen oxidation and evolution reactions of platinum, Nat. Catal. 4 (2021) 711–718.

[50] T.W. van Deelen, C. Hernández Mejía, K.P. de Jong, Control of metal-support interactions in heterogeneous catalysts to enhance activity and selectivity, Nat. Catal. 2 (2019) 955–970.

[51] J.Y. Park, L.R. Baker, G.A. Somorjai, Role of hot electrons and metal-oxide interfaces in surface chemistry and catalytic reactions, Chem. Rev. 115 (2015) 2781–2817.

[52] Y.F. Xu, P.N. Duchesne, L. Wang, A. Tavasoli, A.A. Jelle, M. Xia, J.F. Liao, D. B. Kuang, G.A. Ozin, High-performance light-driven heterogeneous CO₂ catalysis with near-unity selectivity on metal phosphides, Nat. Commun. 11 (2020) 5149.

[53] M. Fu, X. Li, Z. Zhang, Comparative study of optical properties by clay minerals with magnetic coating in colloidal dispersion under an external magnetic field, Appl. Clay Sci. 181 (2019), 105224.

[54] C. Kim, S. Hyeon, J. Lee, W.D. Kim, D.C. Lee, J. Kim, H. Lee, Energy-efficient CO₂ hydrogenation with fast response using photoexcitation of CO₂ adsorbed on metal catalysts, Nat. Commun. 9 (2018) 3027.

[55] S. Luo, X. Ren, H. Lin, H. Song, J. Ye, Plasmonic photothermal catalysis for solar-to-fuel conversion: current status and prospects, Chem. Sci. 12 (2021) 5701–5719.

[56] S. Luo, H. Lin, Q. Wang, X. Ren, D. Hernández-Pinilla, T. Nagao, Y. Xie, G. Yang, S. Li, H. Song, M. Oshikiri, J. Ye, Triggering water and methanol activation for solar-driven H₂ production: Interplay of dual active sites over plasmonic ZnCu alloy, J. Am. Chem. Soc. 143 (2021) 12145–12153.

[57] H. Song, X. Meng, Z.-j Wang, Z. Wang, H. Chen, Y. Weng, F. Ichihara, M. Oshikiri, T. Kako, J. Ye, Visible-light-mediated methane activation for steam methane reforming under mild conditions: A case study of Rh/TiO₂ catalysts, ACS Catal. 8 (2018) 7556–7565.

[58] H. Song, X. Meng, T.D. Dao, W. Zhou, H. Liu, L. Shi, H. Zhang, T. Nagao, T. Kako, J. Ye, Light-enhanced carbon dioxide activation and conversion by effective plasmonic coupling effect of Pt and Au nanoparticles, ACS Appl. Mater. Interfaces 10 (2018) 408–416.

[59] H. Ge, Y. Kuwahara, K. Kusu, Z. Bian, H. Yamashita, Ru/HₓMoO₃₋ᵧ with plasmonic effect for boosting photothermal catalytic CO₂ methanation, Appl. Catal. B-Environ. 317 (2022), 121734.

[60] L. Wang, Y. Dong, T. Yan, Z. Hu, A.A. Jelle, D.M. Meira, P.N. Duchesne, J.Y.Y. Loh, C. Qiu, E.E. Storey, Y. Xu, W. Sun, M. Ghoussoub, N.P. Kherani, A.S. Helmy, G. A. Ozin, Black indium oxide a photothermal CO₂ hydrogenation catalyst, Nat. Commun. 11 (2020) 2432.

[61] E. Abdullayev, A. Joshi, W. Wei, Y. Zhao, Y. Lvov, Enlargement of halloysite clay nanotube lumen by selective etching of aluminum oxide, ACS Nano 6 (2012) 7216–7226.

[62] Y. Song, P. Yuan, P. Du, L. Deng, Y. Wei, D. Liu, X. Zhong, J. Zhou, A novel halloysite–CeOₓ nanohybrid for efficient arsenic removal, Appl. Clay Sci. 186 (2020), 105450.

[63] B. Xie, R.J. Wong, T.H. Tan, M. Higham, E.K. Gibson, D. Decarolis, J. Callison, K.-F. Aguey-Zinsou, M. Bowker, C.R.A. Catlow, J. Scott, R. Amal, Synergistic ultraviolet and visible light photo-activation enables intensified low-temperature methanol synthesis over copper/zinc oxide/alumina, Nat. Commun. 11 (2020) 1615.

[64] Z. Wang, H. Song, H. Pang, Y. Ning, T.D. Dao, Z. Wang, H. Chen, Y. Weng, Q. Fu, T. Nagao, Y. Fang, J. Ye, Photo-assisted methanol synthesis via CO₂ reduction under ambient pressure over plasmonic Cu/ZnO catalysts, Appl. Catal. B-Environ. 250 (2019) 10–16.

[65] S. Kattel, P. Liu, J.G. Chen, Tuning selectivity of CO₂ hydrogenation reactions at the metal/oxide interface, J. Am. Chem. Soc. 139 (2017) 9739–9754.

[66] S. Song, H. Song, L. Li, S. Wang, W. Chu, K. Peng, X. Meng, Q. Wang, B. Deng, Q. Liu, Z. Wang, Y. Weng, H. Hu, H. Lin, T. Kako, J. Ye, A selective Au-ZnO/TiO₂ hybrid photocatalyst for oxidative coupling of methane to ethane with dioxygen, Nat. Catal. 4 (2021) 1032–1042.

[67] Y. Qi, L. Song, S. Ouyang, X. Liang, S. Ning, Q.Q. Zhang, J. Ye, Photoinduced defect engineering: enhanced photothermal catalytic performance of 2D black In₂O₃₋ₓ nanosheets with bifunctional oxygen vacancies, Adv. Mater. 32 (2019) 1903915.

[68] C. Song, X. Liu, M. Xu, D. Masi, Y. Wang, Y. Deng, M. Zhang, X. Qin, K. Feng, J. Yan, J. Leng, Z. Wang, Y. Xu, B. Yan, S. Jin, D. Xu, Z. Yin, D. Xiao, D. Ma, Photothermal conversion of CO₂ with tunable selectivity using Fe-based catalysts: from oxide to carbide, ACS Catal. 10 (2020) 10364–10374.